Ocean Dynamics (2006) 56: 525–542
DOI 10.1007/s10236-005-0054-x

Jean-Baptiste Sallée · Nicolas Wienders · Kevin Speer · Rosemary Morrow

Formation of subantarctic mode water in the southeastern Indian Ocean

Received: 20 July 2005 / Accepted: 7 December 2005 / Published online: 7 February 2006

Abstract Subantarctic Mode Water (SAMW) is the name given to the relatively deep surface mixed layers found directly north of the Subantarctic Front in the Southern Ocean, and their extension into the thermocline as weakly stratified or low potential vorticity water masses. The objective of this study is to begin an investigation into the mechanisms controlling SAMW formation, through a heat budget calculation. ARGO profiling floats provide estimates of temperature and salinity typically in the upper 2,000 m and the horizontal velocity at various parking depths. These data are used to estimate terms in the mode water heat budget; in addition, mode water circulation is determined with ARGO data and earlier ALACE float data, and climatological hydrography. We find a rapid transition to thicker layers in the central South Indian Ocean, at about 70°S, associated with a reversal of the horizontal eddy heat diffusion in the surface layer and the meridional expansion of the ACC as it rounds the Kerguelen Plateau. These effects are ultimately related to the bathymetry of the region, leading to the seat of formation in the region southwest of Australia. Upstream of this region, the dominant terms in the heat budget are the air–sea flux, eddy diffusion, and Ekman heat transport, all having approximately equal importance. Within the formation area, the Ekman contribution dominates and leads to a downstream evolution of mode water properties.

Responsible Editor: Bernard Barnier

J. B. Sallée (✉) · R. Morrow
LEGOS-UMR5566,
18 av Edouard Belin,
31401 Toulouse cedex 9, France
e-mail: Jean-Baptiste.Sallee@notos.cst.cnes.fr

N. Wienders · K. Speer
Department of Oceanography, OSB 435,
Florida State University,
Tallahassee FL 32306-4320, USA

Introduction

Mode water is the name given to an ocean layer with physical properties (temperature, salinity) that are nearly homogeneous vertically and horizontally, covering an extended area in a given basin (e.g., Hanawa and Talley 2001), and thus occupying a relatively large volume compared to other water types. Mode waters can be identified by relatively deep surface mixed layers, or, within the water column, by a pycnostad on a density–depth plot, or by a minimum of large-scale potential vorticity (PV). They are one of the primary results of air–sea interaction (Speer et al. 1995) and serve to ventilate the interior of the upper ocean as they spread within gyres and boundary currents (McCartney 1982; Hanawa and Talley 2001).

In the Southern Ocean, Subantarctic Mode Water (SAMW) is formed when winter cooling leads to convection and the formation of a deep mixed layer just north of the Subantarctic Front (SAF) (McCartney 1977). In the Indian Ocean, as in the Atlantic and Pacific Oceans, SAMW then enters the thermocline by advection and diffusion ("spreading") where it becomes part of central waters and contributes to ventilating the thermocline. Oxygen-rich layers thus formed may persist to the tropics (McCartney 1982). These waters progress in density (and decreasing temperature) from west to east culminating in the formation of Antarctic Intermediate Water in the southeast South Pacific Ocean.

Recently, the role of the SAMW in the climate system has been brought to light, both directly, via observed changes in the temperature, salinity, and CO2 of mode water thought to be related to climate change (e.g., Wong et al. 1999; Sabine et al. 2004), and indirectly, by the physical and biological controls on CO_2 fluxes into and out of this water mass (Sarmiento and Orr 1991; Caldeira and Duffy 2000; Sarmiento et al. 2004; Metzl et al. 1999). We need to understand the formation mechanisms for SAMW, in particular which processes set their hydrological and biogeochemical properties, to answer fundamental question about the carbon and nutrient cycles and the evolution of these cycles in the context of climate change.

Talley's (1999) map of mixed layer oxygen saturation shows an onset of higher oxygen in the southern Indian Ocean at about 70°E, which supports the idea that the southeast Indian Ocean is a dominant source region of mode water; McCarthy and Talley (1999) (see also Keffer 1985) show a low PV pool at 26.8 sigma–theta centered near 90°E,40°S, which is generated by relatively deep winter mixed layers that spreads into the subtropical Indian Ocean. The low PV pool also extends in a narrow tongue eastward south of Australia, a pattern which becomes more pronounced at slightly greater density.

Karstensen and Quadfasel (2002) examined the subduction of water into the south Indian Ocean thermocline because of the horizontal circulation and to Ekman pumping, showing a roughly equal partition between the two components. Mode water formation by air–sea fluxes was estimated and shown to be comparable to net subduction rates. The rough agreement between geostrophic, Ekman, and buoyancy-driven fluxes suggested to them that eddy contributions are generally unimportant. Based on silica concentrations at the base of the mixed layer, they suggested that transport across the SAF was a significant source of mode water.

The northward spreading of mode water into the subtropical gyre is presumably due to northward advection, itself a partial result of the fluxes that create mode water. Stramma (1992) showed that southeast of Africa, the Subtropical Front (STF) is associated with a geostrophic transport of some 60 Sv (1 Sv=106 m^3 s^{-1}) and that this transport is reduced to less than 10 Sv as Australia is

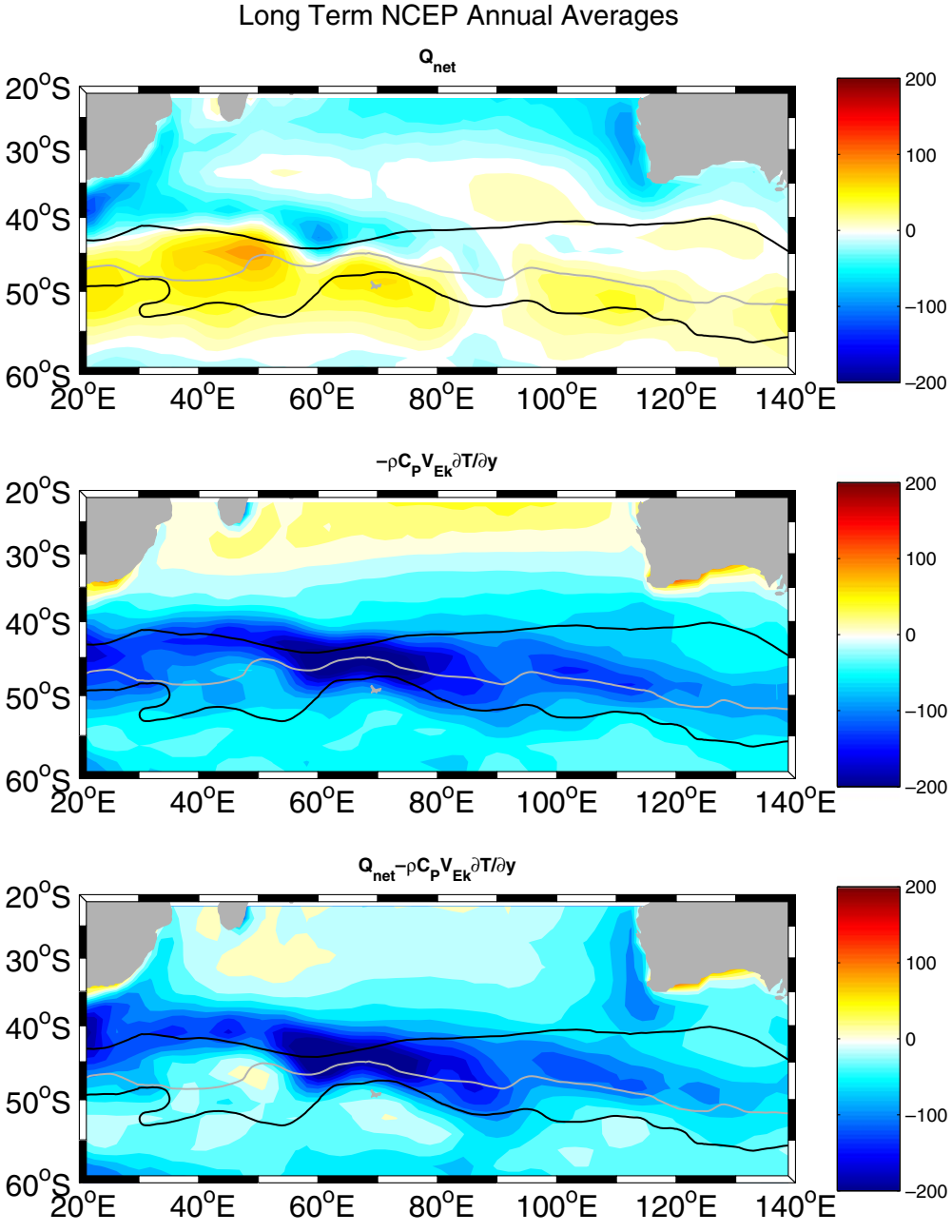

Fig. 1 Climatological average (in W m^{-2}) of net heat flux (*upper*), Ekman heat transport (*middle*), and their sum (*lower*) averaged over the entire NCEP record (1948–2005). *Contours* show the position of the STF, SAF (*gray*), and Polar Front from Orsi et al. (1995)

approached. South of Australia, the strength of the STF decreases further, reaching negligible magnitude near 130° E (Schodlock et al. 1997). The cooling and densification of the water between the STF and SAF across the southern Indian Ocean is associated with the development of northward thermal wind, thus, gradually carrying away water from the northern side of the ACC and into the subtropical gyre.

The question concerning the mechanism for cooling and densification arises: Are air–sea fluxes consistent with this evolution or are other processes acting? According to the National Centers for Environmental Prediction (NCEP) reanalysis, the annual average air–sea flux tends to heat the surface of the ocean in the region between the Polar Front and STF, but if the Ekman heat transport (defined below) is taken into account, the net effect is broad cooling (Fig. 1). Ribbe (1999) has shown, in idealized contexts, how the Ekman transport can modify the temperature–salinity (T–S) characteristics of water in the Southern Ocean. Rintoul and England (2002) estimated a dominant contribution of Ekman heat advection to observed variability in SAMW characteristics the south of Australia, and suggested that Ekman fluxes might partly explain a gradual cooling and freshening across the Indian and Pacific Oceans. Speer et al. (1995) also inferred a strong Ekman contribution to SAMW formation. Our principal goal is to evaluate the contribution of the different terms of the mode water heat budget in the south Indian Ocean using a variety of data sources, but principally ARGO and satellite data. Previous studies did not have access to heat content on the space and time scales of the seasonal development of mode water and could not directly relate fluxes to changes in mode water properties.

Circulation of the southern Indian Ocean

To consider the dynamics of SAMW in the southeast Indian sector, we begin with a discussion of the general upper ocean circulation of the southern Indian Ocean, as summarized in the schematic of Fig. 2. SAMW forms in the deep winter mixed layers in the Subantarctic Zone, north of the SAF, and south of the STF. Downstream of the Kerguelen Plateau near 80°E, the main fronts diverge; the STF moves northward, whereas the main branch of the SAF follows the northern flank of the Southeast Indian Ridge (Sandwell and Zhang 1989) (Fig. 2). This is the region of deepest winter mixed layers described by Talley (1999), McCarthy and Talley (1999).

Fine (1993) divided Indian Ocean SAMW into three density ranges: $26.65 - 26.7\sigma_\theta$, which dominates in the southwestern region, $26.7 - 26.8\sigma_\theta$, which dominates in the central region, and $26.8 - 26.85\sigma_\theta$, which dominates in the south eastern region. These divisions are presumably related to circulation, influenced by the warm, salty Agulhas Return waters upstream, which are continually cooled, freshened and densified by the northward Ekman advection of Antarctic Surface waters along its path (Rintoul and England 2002) (see Fig. 2), and by other processus such as

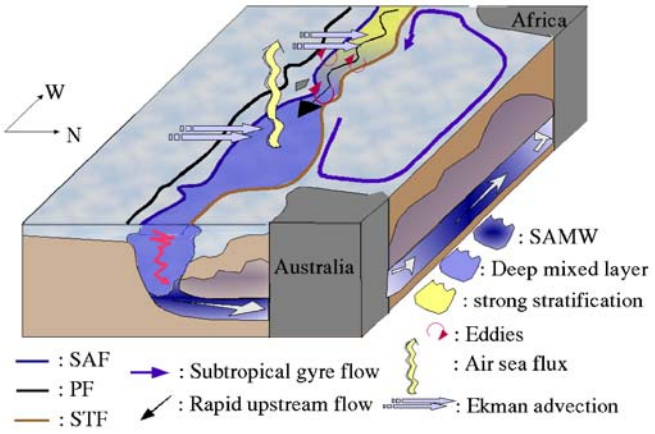

Fig. 2 Schematic of SAMW formation showing the main forcing mechanisms and the relation between the circulation and the region of deep winter mixed layers

air–sea fluxes and eddy mixing. The identification of different mode water density horizons seems to imply distinct formation areas and possibly different forcing mechanisms.

Figure 3 shows a climatological average of velocities at 400-m depth deduced from an objective analysis of ARGO and PALACE floats in the southern Indian Ocean (cf. Appendix I). The meandering Agulhas Return Current is centered around 40°S with velocities greater than 40 cm s^{-1} at 400-m depth. In this analysis, the Antarctic Circumpolar Current (ACC) bifurcates upstream of the Crozet Plateau (55°E) at 40°S, the northern branch merging with the Agulhas Return Current, and the southern branch continuing eastward. Further downstream, this eastward branch bifurcates again between the Crozet Plateau and the Kerguelen Plateau (80°E) (Fig. 3). The main southerly branch continues eastward across the plateau, merging with the flow downstream of the plateau. This circulation pattern is also indicated by the Surface Velocity Program drifters (not shown). The merging of ACC and the Agulhas waters upstream of the two plateaus points to preferred regions of water mass mixing.

The bathymetry clearly has a direct impact on the circulation in this region, creating large permanent meanders of the Agulhas Return Current and the ACC, and limiting the latitudinal excursions of the hydrological fronts (see Fig. 3). North of the ACC, distinct interior recirculation regimes exist related to bathymetry that may set the primary mode water divisions. Within the ACC, the Crozet Plateau and the Kerguelen plateau strongly control the frontal positions in the south Indian Ocean, and the SAF and the STF converge north of these plateaus (Figs. 2 and 3). In the southeastern sector downstream of the Kerguelen Plateau, these two fronts diverge, giving rise to a large area of reduced flow (Fig. 3) where the SAMW forms.

Finally, strong eddy activity is associated with instabilities of the main currents described above. The Agulhas Current System to the west has the highest eddy kinetic energy (EKE) of the global ocean, and EKE maximums are located along the main axes of the meandering Agulhas Return Current and the ACC (Le Traon and Morrow 2001).

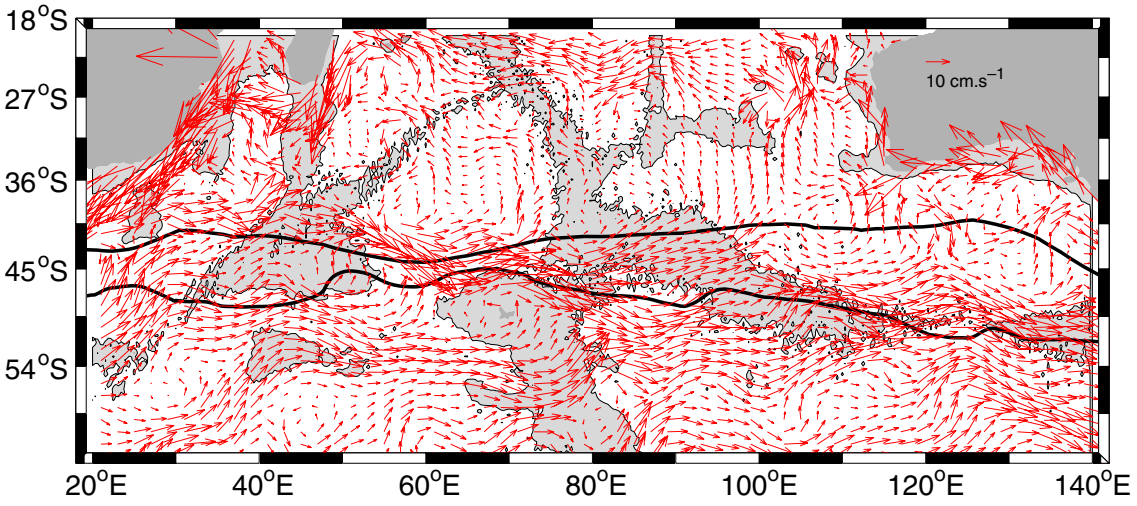

Fig. 3 Averaged velocities at 400 m depth deduced from an objective analysis of ARGO and PALACE floats in the southern Indian Ocean (cf. Appendix III). Bathymetry less than 3,500 m depth is shaded *gray*. *Solid lines* indicate the STF (north) and the SAF (south) from Orsi et al. (1995)

Eddy mixing can be important in the diffusion of tracers (Davis 1991), and in the transport of properties across the SAF (Karstensen and Quadfasel 2002).

In the following analysis, we will consider how these different dynamics and forcing mechanisms influence the surface heat budget in the region of SAMW formation downstream of the Kerguelen Plateau. We start by the heat budget because we have good surface temperature fields, which allow us to accurately calculate the spatiotemporal evolution of the temperature gradients. Unfortunately, accurate surface salinity measurements are not available on the same space and time scales to estimate a similar surface salinity budget, but we will address the role of salinity in the discussion.

Data

Profiling floats

The vertical structure of the ocean is obtained in this study using the ARGO data set. The ARGO float program has seeded all of the world's ocean for several years particularly the Southern Ocean, which historically is poorly sampled. Good data coverage in the southern Indian Ocean started in late 2002, and this study focuses on the years 2003 and 2004. These data were collected and made freely available by the International Argo Project and the national programs that contribute to it.[1] We only used profiles that passed the ARGO real-time quality control, containing information on their position, date, T and S profiles, with their first measurement point shallower than 20 m. According to Wong et al. (2003), the accuracy of the Argo salinity data in the southern Indian Ocean is better than 0.01–0.03 psu, which in our case is sufficient for defining the mixed layer characteristics. PALACE data (Davis 2005) were combined with ARGO floats to compute the mean flow in the southern Indian Ocean (cf Appendix I).

Air–sea fluxes and winds

For the heat budget calculation, we will compare different surface forcing fields. We use the monthly NCEP reanalysis on a 2° grid to estimate the air–sea heat flux. These data are made available by the NOAA-CIRES Climate Diagnostic Center.[2] Two different wind products will be used: monthly averaged winds computed from the NCEP reanalysis, and higher resolution monthly Quickscat gridded winds on a 0.5° grid, available on the IFREMER Cersat (French Satellite Processing and Archiving Facility) website.[3]

Sea-surface temperature

We also use two different Sea Surface Temperature (SST) fields. Monthly Reynolds SST on a 1° grid are used in the climatological analyses, distributed by the NOAA-CIRES Climate Diagnostic Center. For the higher resolution analysis, we use a global satellite SST product (0.25°×0.25°) computed by a combination of the two satellites TMI and AMSR, made available by Remote Sensing Systems.[4]

Surface drifter

Satellite-tracked surface drifter data are used to compute a parameterization of the lateral eddy diffusion coefficient.

[1] http://www.ifremer.fr/coriolis/cdc/argo.htm and http://www.argo.ucsd.edu

[2] http://www.cdc.noaa.gov/.

[3] http://www.ifremer.fr/cersat/.

[4] http://www.ssmi.com/.

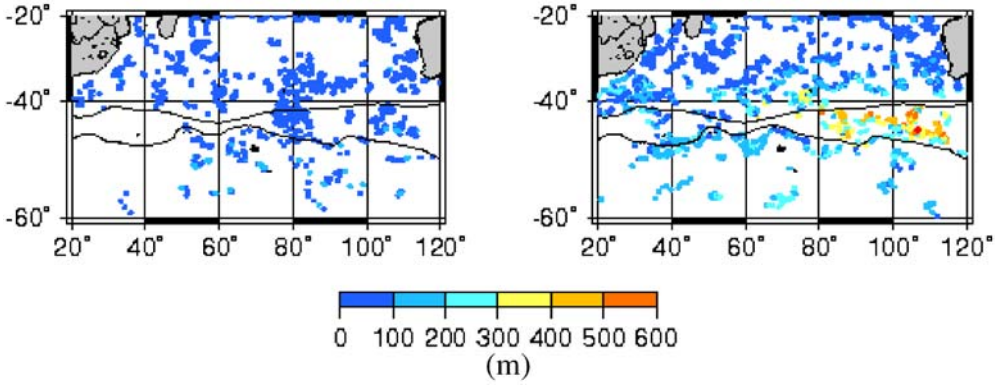

Fig. 4 Mixed layer depth computed from ARGO profiles during 2003 and 2004. The base of the mixed layer is found using a density difference criterion of 0.03 kg m^{-3} (cf. Appendix I). *Solid lines* mark the STF (north) and the SAF (south) from Orsi et al. (1995). *Left panel* Summer profiles (January, February, March). *Right panel* Winter profiles (July, August, September)

This data set is part of the Global Drifter Program/Surface Velocity Program and spans the period 1995–2005 in the southern Indian Ocean. The drifters are equipped with a holey sock drogue at 15-m depth to reduce their surface wind drag. Their positions are determined by ARGOS. The data are received, processed, and distributed by the Atlantic Oceanographic and Meteorological Laboratory (AOML, Miami).[5]

Surface mixed layer properties

The availability of ARGO profile data allows us for the first time to map the evolution of the surface mixed layer properties over large portions of the Indian Ocean and to resolve the seasonal variations.

Figure 4 shows the summer and winter mixed layer depths observed by ARGO profiles during 2003–2004 in the south Indian Ocean. The location of the deep winter convection downstream of the Kerguelen Plateau is clearly illustrated. Figure 5 shows the mixed layer temperature, salinity, and potential density vs longitude between the STF and the Polar Front for all the ARGO profiles during 2003–2004. The properties show a distinct emergence of two branches: a colder, fresher branch of water south of the SAF, and a warmer, saltier branch of water north of the SAF. These branches have relatively shallow winter depths (≤200 m) upstream of 70°E; downstream the deep mixed layers (large dots; Fig. 5) occur in the main mode water formation area.

The existence of the branches reflects the frontal structure of the region with strong gradients at the surface across the SAF, and it also indicates the evolution of these water masses to a common mode water by lateral exchange. Some of this exchange is accomplished by Ekman transport, and some arises due to lateral eddy mixing. The density of the mode water increases to the east, by a combination of temperature and salinity effects.

A T–S diagram (Fig. 6) of the deeper mixed layers south of 30°S (and greater than 200 m deep) shows the SAMW (near 9°C, 34.6 ppt, sigma 26.8; see Fig. 5) in relation to neighboring winter mixed layers across the entire ACC. Some very dense mixed layers occur at the southern limits of the ARGO data near 60°S, with temperature below 3°C and salinity below 34 ppt. At the warm, salty limit are the mode waters of the subtropical gyre in the western Indian Ocean (sigma 26.5–26.7). The deepest mixed layers are found between this wide range of T and S in a relatively narrow density range, 26.7–26.9. Thus, near-density compensation occurs in the mode water across an extraordinarily large range of T and S, and again points to lateral processes as sources of heat and salt.

In the following sections, we will consider certain characteristics of the surface mixed layer in the formation region of SAMW in the southeast Indian Ocean. Our study region lies north of the SAF and south of the STF, downstream of the Kerguelen Plateau at 70°E and extending eastward to 140°E. The front positions are defined from the vertical ARGO profiles because precise horizontal subsurface gradients are not available. The SAF is defined using the Nagata et al. (1988) definition, as the isotherm 7°C at 100 m. The STF also follows Nagata et al. (1988) and is defined as the isotherm 11°C at 150 m.

Stability at the base of the mixed layer

The mixed layer in the formation region creates the dynamic link between the atmospheric forcing and subsurface mode water layer. Before we start an analysis of the forcing terms for the mixed layer, we will first consider the stability at the base of the mixed layer. Is the base of the mixed layer strongly or weakly stratified throughout the different seasons, and is this stability dominated by a strong thermocline or halocline?

The stability of a water column is characterized by the Brunt–Vaïsala coefficient N defined by: $N^2 = \frac{g}{\rho}\frac{\partial \rho}{\partial z}$. The column is stable if and only if N is positive. The base of the mixed layer is defined using a 0.03-density difference criterion (see Appendix II). Figure 7 shows the evolution of the stability, calculated over a 10-m deep interval at the base of the mixed layer, using the available ARGO floats in the formation region. The strong seasonal cycle remains positive, i.e., the base of the mixed layer is always stable. However, the stability at the base of the mixed layer is weak in winter, indicating that it is close to the threshold allowing deeper convection. A more in-

[5] http://www.aoml.noaa.gov/.

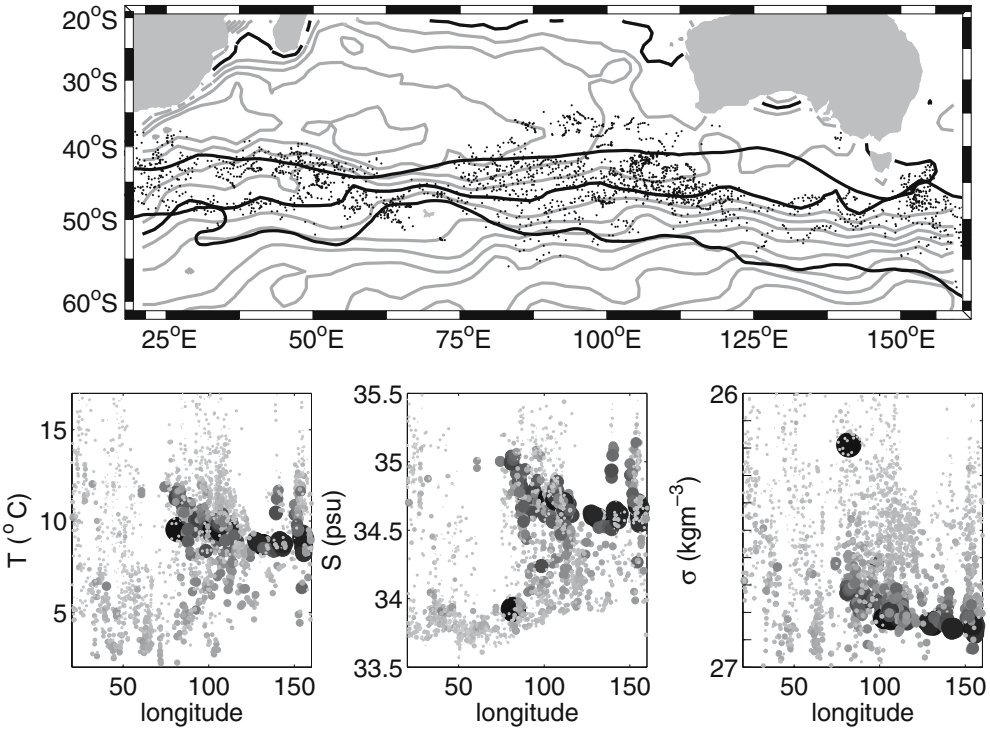

Fig. 5 *Upper panel* Position of all ARGO profiles between the Polar Front and the STF (as defined by the properties of each individual profile). Streamfunction derived from an objective analysis of float positions (Appendix I) is in *graycontours*. *Solid lines* indicate the STF (north) and the SAF (south) from Orsi et al. (1995). *Lower panel* Temperature, salinity, and potential density for each profile displayed as a function of longitude, with symbol size corresponding to mixed layer depth. The evolution of properties along and between the fronts shows a convergence of values on either side of the SAF to form progressively denser mode waters

teresting view comes from splitting this stability calculation into its thermal and haline parts.

The vertical density gradient can be written as a first approximation (Gill 1982):

$$\frac{1}{\rho}\frac{\partial \rho}{\partial z} = -\alpha \cdot \frac{\partial T}{\partial z} + \beta \frac{\partial S}{\partial z}$$

where: $\alpha = \frac{1}{\rho} \cdot \frac{\partial \rho}{\partial T}$ et $\beta = \frac{1}{\rho} \cdot \frac{\partial \rho}{\partial S}$

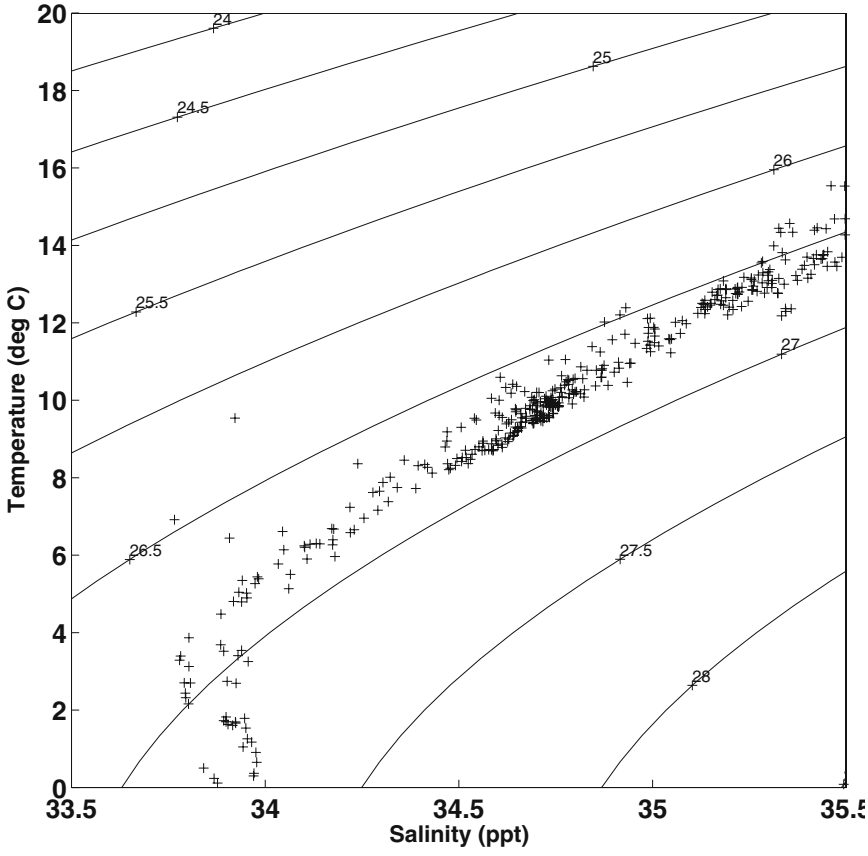

Fig. 6 Temperature–salinity diagram for mixed layers (values at middepth within the layer) greater than 200 m thick, from all ARGO data between 30 S–60 S. Potential density overlaid. SAMW in longitudes 70–120°E is concentrated between 8–10 C and 34.4–34.9 ppt, and 26.7 sigma. Relatively deep mixed layers also exist at neighboring T–S values outside this range; the distinction between mode waters is not absolute, either in T–S space or geographically

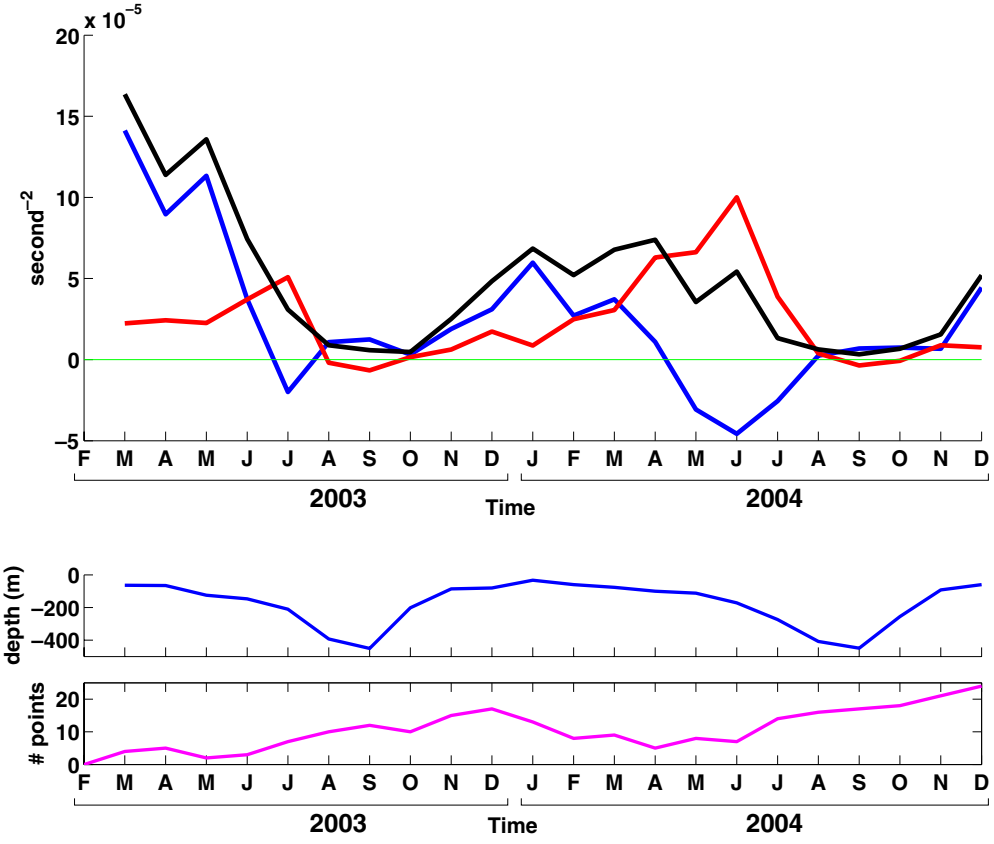

Fig. 7 *Upper panel* Monthly average of the stability (s^{-2}) at the base of the mixed layer computed from the 2003 and 2004 ARGO profiles in the SAMW formation region. The *black line* represents the stability at the base of the mixed layer, i.e., the evolution of the Brunt–Vaïsala coefficient. The *red line* is the haline component of the stability at the base of the mixed layer, i.e., $N_S = g\beta\frac{\partial S}{\partial z}$. The *blue line* is the thermal component. *Middle panel* Monthly averaged mixed layer depth (in meters) computed from the same data. *Lower panel* Monthly number of data points used in the mixed layer stability calculation

The role of the thermal and haline stratification on the stability at the base of the mixed layer is represented by the two terms: $N_T = -g\alpha\frac{\partial T}{\partial z}$ (thermal stability) and $N_S = g\beta\frac{\partial S}{\partial z}$ (haline stability).

The thermal stratification is dominant at the base of the mixed layer for most of the seasonal cycle (Fig. 7). The exception is during early winter, when the base of the mixed layer is strongly destabilized by cooling (the thermal stability term becomes negative in June–July) and the stability is maintained by the haline component (fresher). In late winter (August to October), positive thermal stability at the base of the mixed layer is reestablished and now it is the haline component that tends to destabilize the water column (saltier). We note that during winter, the two terms tend to compensate; that is, the thermal destabilization is compensated by a freshening, and vice versa.

An analysis of the heat budget equation in the mixed layer of the formation region will give us a clearer idea of the seasonal evolution of the forcing terms and their relation to this observed mixed layer destabilization. It is also clear that the salinity terms will play an important role in late winter. To start, we consider the heat budget equation.

Heat budget equation in the mixed layer

For the vertically averaged surface layer, the heat budget can be written:

$$h\left(\frac{\partial T}{\partial t} + \mathbf{v}\cdot\nabla T + \overline{v'\cdot\nabla T'}\right) + \Delta T w_e + \nabla\cdot \int_{-h}^{0}\widehat{v}\widehat{T}dz = \frac{Q_o}{\rho C_p} \tag{1}$$

(e.g., Stevenson and Niiler 1983; Qui 2000), where h is the layer thickness, T the mean (low-passed in time/space) temperature, and $\mathbf{v}$ the mean horizontal velocity vector. Primes denote variability about the mean state, ΔT is the temperature jump at the base of the layer, w_e the entrainment velocity, $\widehat{T}$ and $\widehat{v}$ represent deviations from the vertical average, and Q_o is the net heat flux at the ocean surface. The heat flux across the base of the layer due to shortwave radiative penetration is assumed small for the deep winter mixed layers considered here, and the diffusive flux of heat at the base of the layer is neglected. The role of

vertical temperature deviations within the surface layer associated with small vertical density variation were considered, but found to be small in all instances in this region, hence are also neglected.

Previous studies suggest that Ekman advection and air–sea fluxes are dominant terms in destabilizing the winter water column to create the strong and deep convection observed (Ribbe 1999; Rintoul and England 2002). These studies were based on numerical model outputs or dimensional analysis; in this study, we estimate these terms from the available in situ data. The balance

$$h \cdot \frac{\partial T}{\partial t} = \frac{Q_{net}}{\rho C_p} - V_E \cdot \frac{\partial T}{\partial y} \tag{2}$$

agrees with the simplified model of MacCready and Quay (2001) for the heat balance in the ACC. We will consider this simple balance first.

The temperature evolution and mixed layer depths are calculated from the ARGO data. A critical term in the heat budget equation is h, the depth of the mixed layer. We carried out numerous tests to decide which criterion would be the most appropriate in the present case (Appendix II). The method retained was to use a 0.03-density difference threshold for the determination of the mixed layer depth.

The temperature evolution is calculated for each ARGO float within the formation region, as described in Appendix III. For the calculation, we use pairs of float profiles separated by 30 days (three float cycles) that remain in our zone, and the temperature is integrated down to the deepest mixed layer depth occurring for the two profiles. Thus, the mixed layer depth for our calculation is not fixed but varies in space and time. The heat content variation for each individual float is obtained using those two profiles.

The forcing terms are interpolated onto each ARGO float position and then averaged over the same 30-day period. In other words, considering four consecutive float profiles, Ekman advection, and air–sea flux are interpolated (in time and space) onto the first, the second, and the third profile and then averaged to form the monthly mean. The monthly heat content variation is computed between the first and the fourth profiles (three float cycles).

Comparing climatological and realistic Ekman forcing

We used two different techniques to compute the Ekman term. The first uses classical climatological data sets: NCEP monthly winds and Reynolds monthly SST climatology. We find that the magnitude of the Ekman term is small compared to the analytical predictions (Rintoul and England 2002). For the second Ekman calculation, we use higher resolution Quickscat satellite scatterometry winds and satellite SST fields from TMI/AMSR. The result is surprising: During winter 2003, realistic forcing increases the Ekman component by 30%, from −80 to −110 W m^{-2}, while in winter 2004 it increases by more than 50% from −60 to −130 W m^{-2} (see Fig. 8). The annual mean increases by 10% (from −49.35 to −54 W m^{-2}).

The main reason for this difference is that the Reynolds SST is much too smooth at these latitudes. There are little ship SST data and considerable cloud cover, which blocks the satellite Advanced Very High Resolution Radiometer measurements, and so the Reynolds SST reverts to the climatological mean. In contrast, the microwave TMI/AMSR traverses the clouds, and provides mesoscale SST coverage, which is highly correlated with altimetric observations (not shown). For instance, we frequently observe frontal movements of the SAF associated with meanders or eddy spawning, which are detected by TMI/AMSR but not observed by Reynolds SST. Having strong SST gradients, which are correctly positioned and not too smooth, impacts directly on the Ekman advection calculation (Fig. 9). This also impacts on the temporal evolution: the high-resolution Ekman forcing has a strong seasonal cycle, while the Reynolds–NCEP Ekman calculation is weaker, with a smaller difference between the two calculations for the annual mean. If we spatially average the two products over a region that is large enough, we get comparable results (not shown), suggesting that the large-scale forcing is well-represented. In the following section, we chose to work with the satellite Ekman heat flux based on Quickscat winds and TMI AMSR SST, providing a better local estimate of the Ekman forcing around the individual ARGO floats.

Comparison of the forcing terms

The monthly averages of the different forcing terms are shown in Fig. 8. The annual heating and cooling cycle from the air–sea flux Q is largely responsible for the variations in mixed layer heat content. Very strong cooling is observed in winter in the mixed layer, with mean values of over 200 W m^{-2} heat loss. Half of this heat loss is due to air–sea fluxes (−100 W m^{-2} heat loss on average in winter), and the increased Ekman fluxes in winter also contribute to cooling the mixed layer (by −100 W m^{-2}).

Figure 10 shows the two sides of Eq. 2, as the sum of the air–sea fluxes and the Ekman forcing vs the heat content variation and their associated error bars. The two curves coincide almost throughout the 2-year period, validating our technique and the use of the ARGO data set to calculate the heat content variations. Within the error margin, the sum of the two forcing terms is enough to close the heat budget for this SAMW formation region. We note that this closure is improved by using the high-resolution Ekman term, which increases the forcing term by 30–50% in winter.

The standard deviation of the ARGO heat content evolution is large compared to the forcing terms. This raises the question of whether these monthly averages are representative of all of the floats in our formation region, particularly when we consider that the winter standard deviation of the heat content variation ranges from 0 to

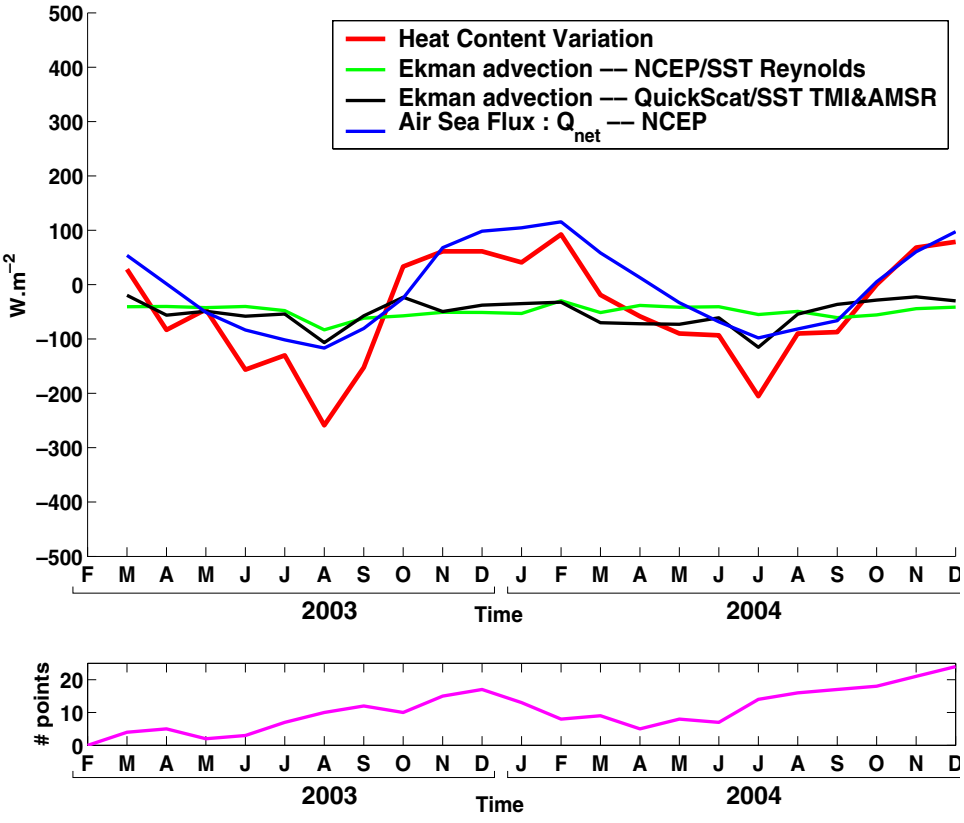

Fig. 8 *Upper panel* Monthly averaged simplified heat budget terms (W m^{-2}) for 2003–2004 in the SAMW formation area. *Red line* heat content variation computed from the ARGO profiles in the formation area. *Blue line* NCEP air–sea heat fluxes. *Green line* Ekman advection calculated using the Reynolds optimal interpolated SST in association with the NCEP winds. *Black line* Ekman advection from the combination of satellite TMI/AMSR SST, and satellite Quickscat winds. *Lower panel* Number of data points used in the monthly heat content calculation

−500 W m^{-2}. In the following section, we will investigate whether the Ekman advection and the air–sea flux are always sufficient to explain the heat content variation in the mixed layer, or whether, for some float conditions, the neglected terms in the simple balance (Eq. 2) become important.

Wintertime heat content

In this section, we consider the detailed heat budget for all of the ARGO float pairs available during the winter 2003 where we found a maximum of heat content variation root mean square (rms). Figure 11 (top panel) shows the two sides of the heat budget (Eq. 2) for all float pairs in our zone, before making the monthly average. There is a good agreement between the two curves; however certain float pairs show large differences; for example, profiles 2, 3, 4, and 5 diverge away from the range of the forcing terms. All of these float pairs are moving in strong SST gradient meanders and may be caught in the energetic eddy and meander propagation north of the front (bottom pannel).

Profile pairs 4 and 5 show a large cooling of the surface layer (down to 500-m depth), whereas profiles 2 and 3 shows warming at depth. Although these float pairs are located north of the SAF following the Nagata et al. (1988) definition, they are clearly influenced by the frontal dynamics, and part of the observed cooling may be due to

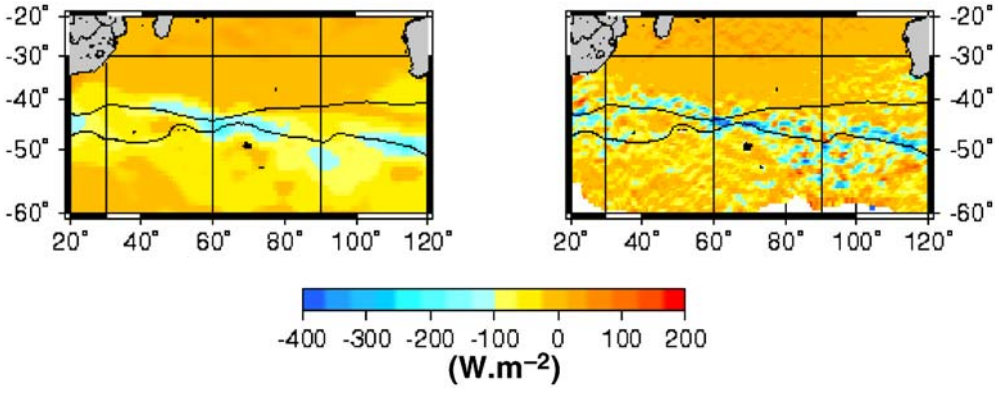

Fig. 9 Mean meridional Ekman advection in August 2003 in the southern Indian Ocean, computed from NCEP reanalyzed winds and Reynolds SST (*left*) and from the combination of Quickscat winds and TMI/AMSR SST (*right*)

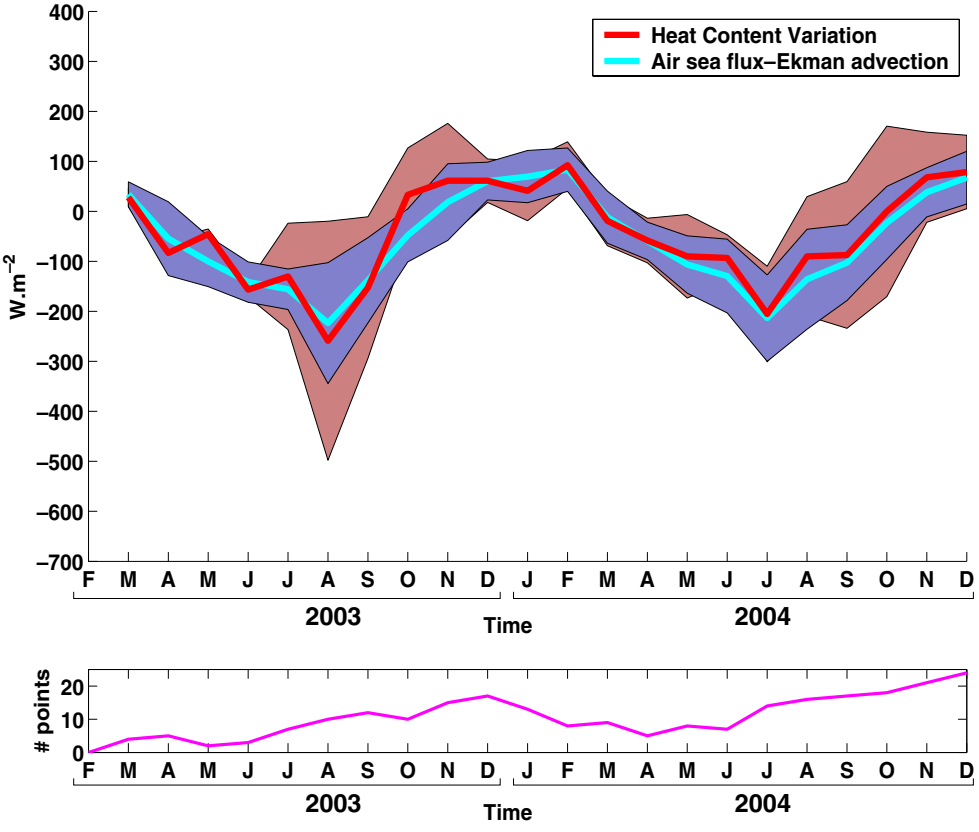

Fig. 10 *Upper panel* Heat balance (Wm^{-2}) for 2003–2004 in the SAMW formation area. *Red line* shows the monthly average of the heat content variation computed from the ARGO profiles in the formation area for the years 2003 and 2004. *Light blue line* is the sum of the high-resolution Ekman advection and air–sea heat fluxes computed around each ARGO profile. *Red and blue shading* represent the standard deviation for the monthly heat content variation and the forcing contributions, respectively. *Lower panel* Number of data points used in the monthly heat content calculation

cross-frontal exchange with the cooler Polar Frontal Zone water masses. For these cases, the difference in the two heat budget curves is not simply due to increased Ekman transport of cooler, fresher surface waters, but may be influenced by geostrophic or eddy advection terms over greater depth.

This focus on the 2003 winter case highlights two important features. For most of the float pairs, which remain in a fairly homogeneous subantarctic water mass, the simple balance of air–sea heating plus meridional Ekman flux is sufficient to explain the heat content variation over a 1-month period, even during winter. However, certain float pairs that are situated close to the SAF or its meanders can exhibit large heat content variations that are not explained by this simple balance, suggesting that the floats may also move across eddies and meanders of the mean flow. These cases can have a large impact on our monthly averages—without the four extreme cases in winter 2003, the average heat content evolution would be around −190 W m^{-2}, rather than the observed −260 W m^{-2}. We know that the float sampling is not completely random—Lagrangian floats tend to converge toward the more energetic regions (Davis 1991) and are especially influenced by the deep-reaching meanders and eddies of the SAF. So these extreme cases will be more numerous in our ARGO data than if we had made a homogeneous Eulerian sample of the formation region. On the other hand, these cross-frontal exchanges are also a key mechanism in bringing deep cool, fresh layers into the formation region.

Role of the eddy diffusion term

We suspect that eddy fluxes (due to mesoscale eddies or meanders of the front) may be important close to the energetic SAF for the heat balance equation. To investigate this further, we replace the missing $h\overline{v'\nabla T'}$ term from Eq. 1 by a simple Laplacian form to parameterize the eddy heat diffusion, $K_h\nabla^2 T$. We have computed a climatological average of the lateral eddy diffusion coefficient K_h in 5° by 5° bins following Davis (1991) (see also Oh et al. 2000),[6] using the available surface drifter data from 1995 to 2005 over the Indian Ocean. Mean eddy heat diffusion in W m^{-3} is then calculated using the relation: $\rho C_p K_h \nabla^2 <T>$; $<T>$ is the mean SST derived from 3 years of high-resolution TMI-AMSR data.

This surface eddy heat flux estimate based on surface drifter data (Fig. 12) is consistent with the results of Gille (2003b) and indicates that the maximum eddy heat diffusion occurs upstream of the Crozet Plateau and Kerguelen Plateau, where the STF and the SAF converge between 60 and 70°E.

[6] The eddy diffusion coefficient has been computed using the single particle diffusivity tensor relation described by Davis (1991): $k_{jk}(\mathbf{x} = \langle v_j'(t_0|\mathbf{x}, t_0) d_k'(t_0 - t|\mathbf{x}, t_0)\rangle$, where v' and d' are the departures from the Lagrangian mean velocity and displacement, respectively; t_0 is the initial time and the brackets indicate averaging over the ensemble of the particles; the notation a $(t|\mathbf{x}_0, t_0)$ represents the value of a at time t of a particle passing through $\mathbf{x}_0$ at time t_0.

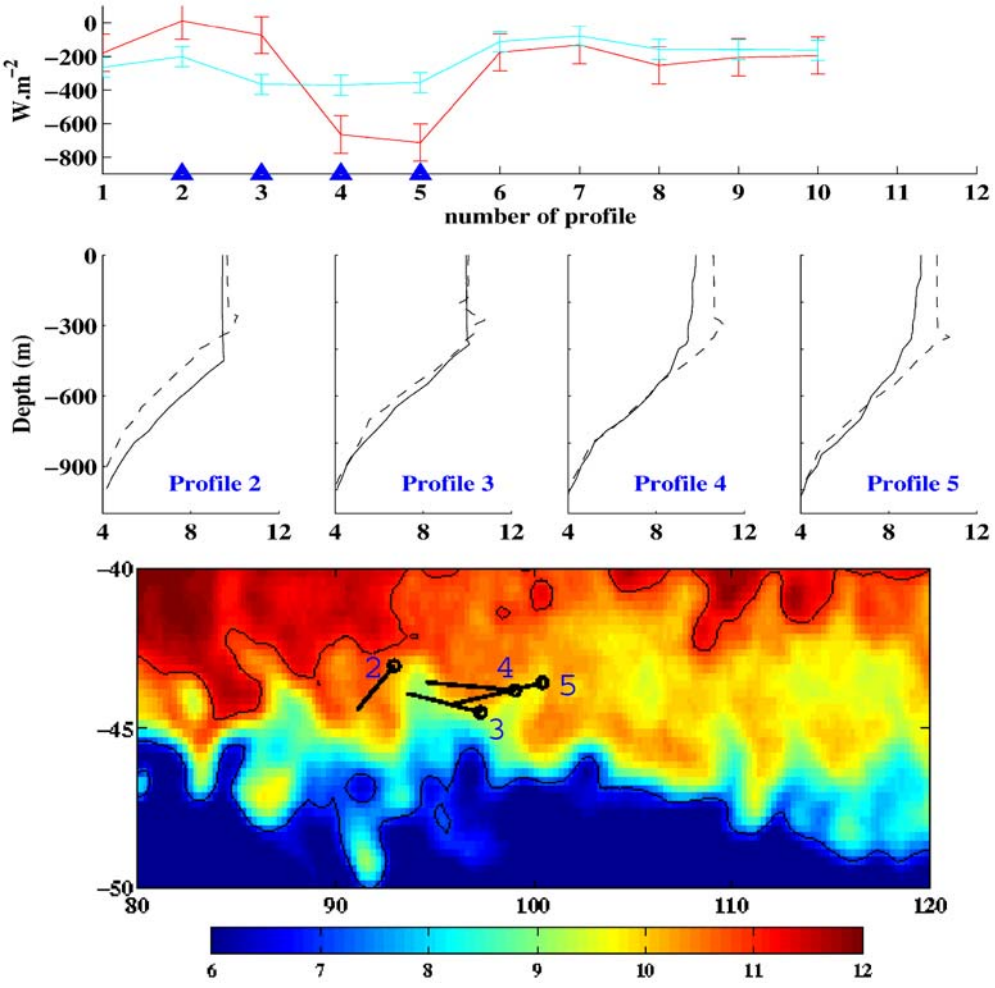

Fig. 11 Details of the individual winter heat budget terms included in the August 2003 monthly average. *Upper panels* The ARGO heat content variation (*red line*) and the associated forcing contributions (Ekman advection + air–sea fluxes) (*light blue line*), which were used in the monthly average presented in Fig. 10. *Error bars* are the 2003/2004 rms of heat content variation (*red*) and forcing contribution (*light blue*). *Middle panel* Pairs of profiles where we found a large difference between heat content variation and forcing contribution. The *dashed* profile is 1 month before the *solid* profile. The difference between them is the heat content in the mixed layer. *Lower panel* Geographical position of previous profiles. The *circle* denotes the profile corresponding to the *solid line*. *Colorcontours* of SST for 15 August 2003 are shown. *Black curves* are the 7 and 11°C coutours

In the region of SAMW formation downstream of Kerguelen, the eddy heat diffusion is weaker. This confirms our results from the previous section, where we saw only a few cases in the monthly average, which were influenced by mesoscale eddies and possible stronger eddy diffusion. Karstensen and Quadfasel (2002) also proposed that eddy fluxes were not important for the generation and subduction of mode water because air–sea flux based estimates agreed with kinematic models. However, their results were by construction averaged over all of the density outcrop area, that is, averaged over longitude too, which tends to average out the eddy flux. Our results indicate that eddy heat

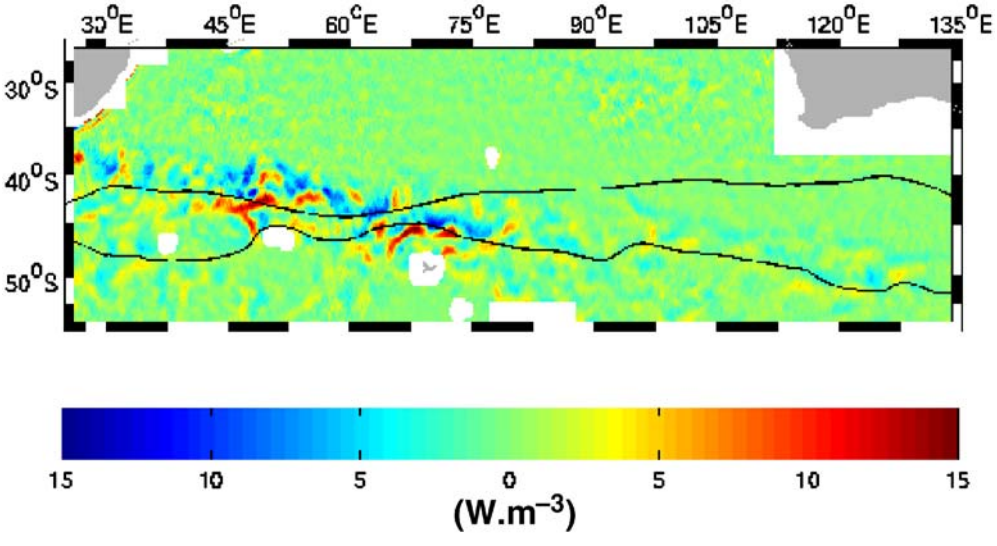

Fig. 12 Lateral surface eddy heat flux in the southern Indian Ocean (in W m^{-3}) from surface drifter and averaged TMI/AMSR SST. *Solid lines* indicate the STF (north) and the SAF (south) from Orsi et al. (1995)

diffusion is also weak in the seat of SAMW formation. However, there is substantial variation of eddy diffusion along the fronts, and importantly, just upstream of Kerguelen Plateau. We will now consider how the along path variations in mixed layer properties and eddy diffusion may control the location of mode water formation.

Longitudinal variation of mixed layer properties

In this section, we consider the circulation around the Crozet and Kerguelen Plateaux in more detail. Figure 3 showed that branches of the ACC bifurcate to the north and merge with the Agulhas Return Current near Crozet Island at 50°E, and upstream and downstream of the Kerguelen Plateau. Near 60°E and 75°E. These branches appear to be topographically controlled and bring cold, fresh Antarctic water from the south of the SAF in contact with the warm, salty subtropical water asssociated with the Agulhas Return current.

To illustrate how the water column is modified in these merging areas, we will examine the alongstream properties of a composite of two ARGO floats (WM0 No. 1900042 and 1900164), which remained north of the SAF and sampled from upstream of the Crozet Plateau to downstream of Kerguelen (Fig. 13). The first float (WM0 No. 1900164) drifted from 40 to 83°E during September 2004 to September 2005, while the second float (WM0 No. 1900042) drifted downstream from December 2004 to September 2005. Hence, this composite permits an analysis

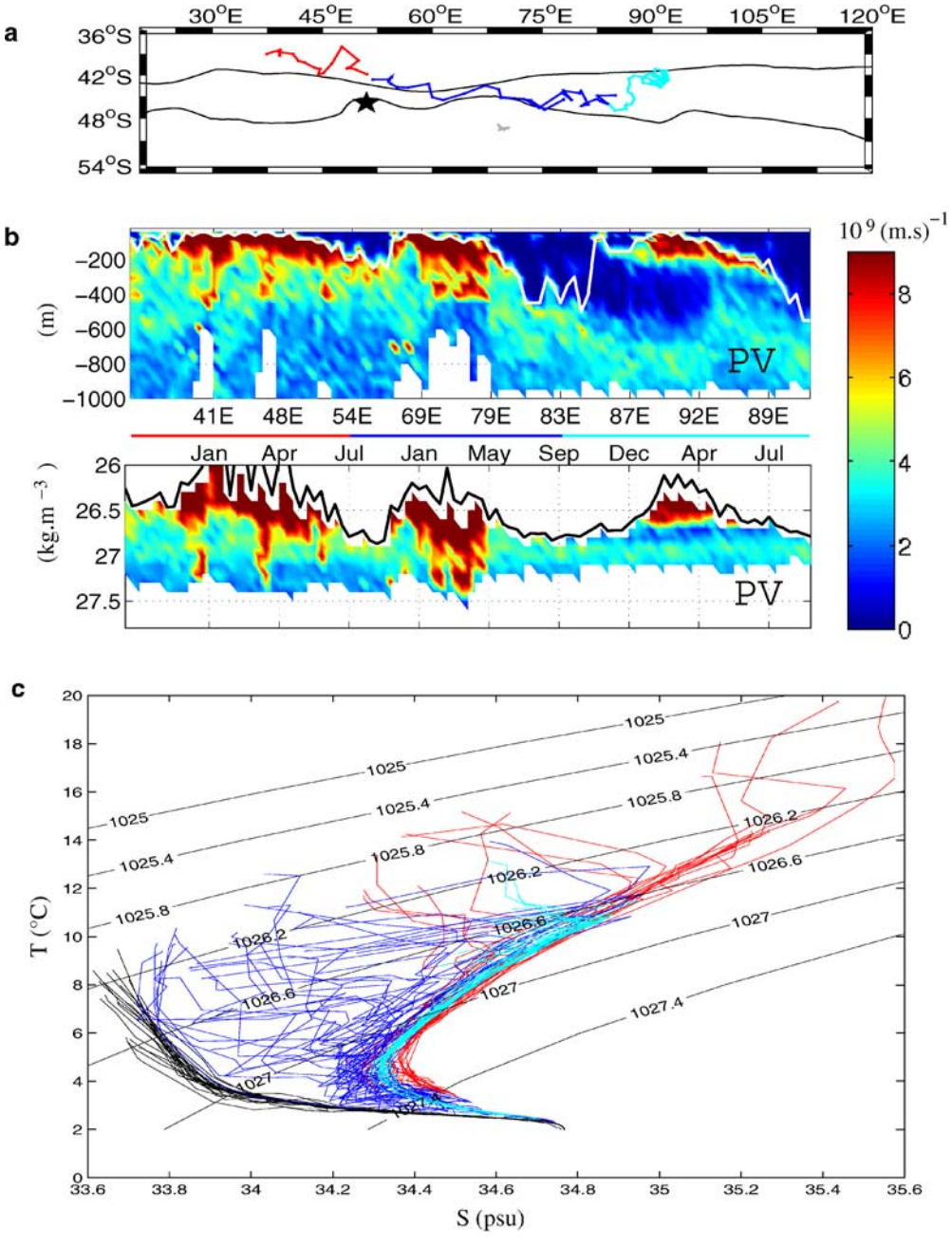

Fig. 13 Vertical structure analyses upstream and downstream of the Kerguelen Plateau from a composite of 2 ARGO float (WM0 No. 1900042 and No. 1900164). **a** Position map of the profiles analyzed. *Colors* are linked with the T–S plot (*lower panel*). The *black star* corresponds to the region were we picked the profiles from the South of the SAF in the T–S analysis. **b** Temporal evolution of the Potential vorticity (m^{-1} s^{-1}) profiles along the float trajectory. The *horizontal axis* is time in "month"; *vertical axis* represents depth in meters. **c** Four regions have been chosen to illustrate the evolution of the water column's hydrological characteristics (T/S) from west to east. Temperature in °C, Salinity in psu, and density in kg m^{-3}. *Colors* are linked to the position map; *black profiles* correspond to the *black star* region in the position map

of the longitudinal evolution of the water column during three seasonal cycles.

To identify the intense mixing region, we have divided the composite track into three parts: profiles from upstream of Crozet are in red, from 55 to 80°E are in blue, and profiles from the mode water formation area downstream are in light blue. In addition to this composite, we also show profiles from south of the SAF (black star; Fig. 13). We will also consider the longitudinal evolution of the forcing terms in the simplified heat Eq. 2, including an extra climatological eddy diffusion term. The annual mean forcing terms are averaged between the SAF and the STF (as defined by Orsi et al. 1995) in 10° longitude bins (Fig. 14).

1. Upstream of Crozet (red profiles), there is a strong vertical stratification below the surface mixed layer, with PV≥50.10^{-9}(m^{-1} s^{-1}) (Fig. 14b). During winter, the mixed layer deepens to 200 m deep with a density of 26.8 kg m^{-3}, which is within the mode water density class. However, it appears that the strong vertical density gradient beneath the mixed layer prevents deeper convection in winter. Furthermore, although the lateral eddy heat fluxes are strong in this region (Fig. 12), the climatological eddy heat diffusion is positive between the fronts (Fig. 14), inducing an annual mean diffusive warming, which opposes the net Ekman cooling.
2. Between the Crozet and Kerguelen Plateaux (blue profiles), we observe a sharp reversal of the eddy heat diffusion term (see Fig. 14), which becomes strongly negative. In this region, the annual mean Ekman and eddy diffusion terms both contribute to cool the mixed layer. Although the eddy heat diffusion term is a climatological parameterization, we can see the impact of the eddy mixing in the individual profiles, which show strong interleaving from the surface down to the deep water density class (≥27.4 kg m^{-3}) (Fig. 13c). The blue profiles show a tendency toward density-compensating interleaving between water masses from south of the SAF (black profiles) and from the northern branch (red profiles). We note that the stratification at 27.2 kg m^{-3} is associated with the salinity minimum linked to intermediate water, which appears to be modified and freshened by the increased mixing in this region (see temperature–salinity plot; Fig. 13c).
3. Downstream of Kerguelen, the fronts separate and the circulation slows. We know from Figs. 5 and 13 that

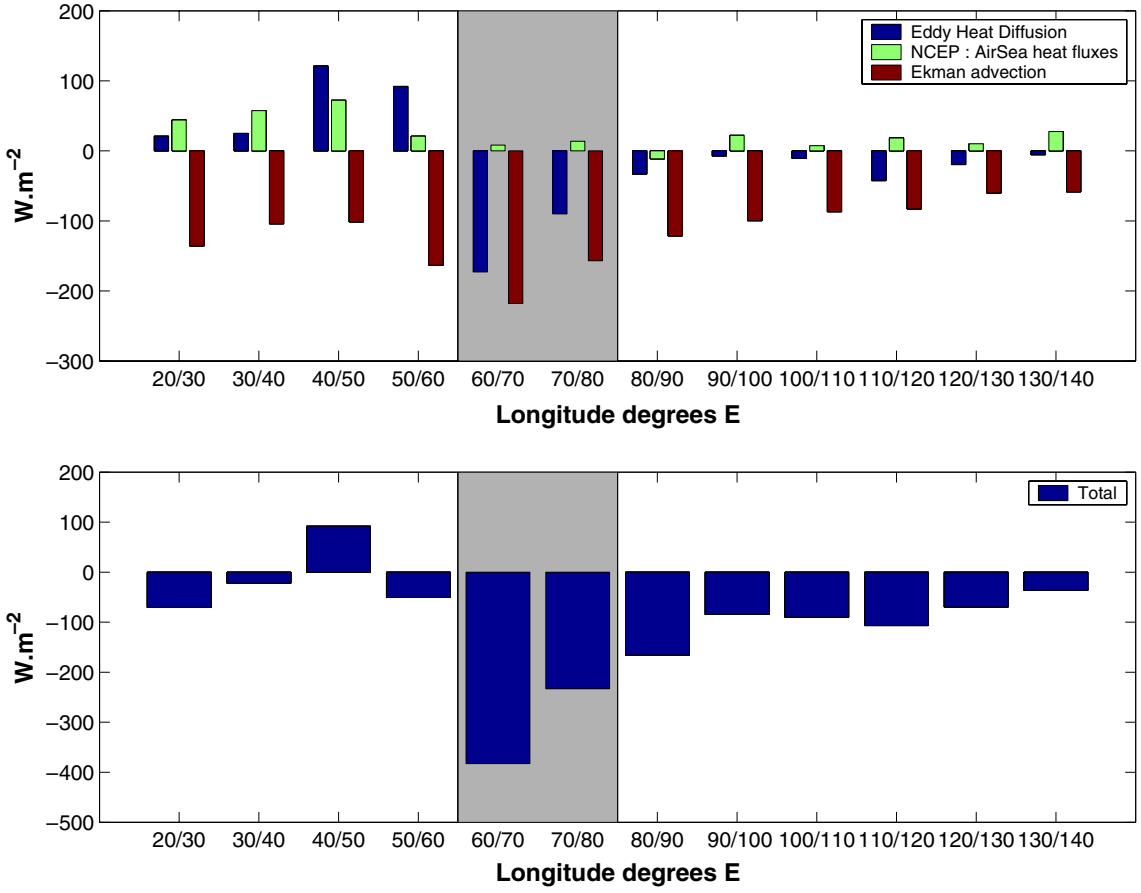

Fig. 14 Longitudinal evolution of the annual mean heat budget forcing contributions averaged between the STF and SAF (fronts defined by Orsi et al. 1995). Ekman advection and air–sea fluxes are computed from long-term NCEP averages; eddy heat diffusion is computed as described in Section 6.4 from surface drifter and satellite SST data. *Grayshading* indicates the Kerguelen Plateau region

the surface mixed layer properties converge toward a more homogeneous density, which is fresher and cooler than upstream. Figure 13c also suggests that the mode and intermediate water masses (light blue profiles) have tighter T–S curves and tend to be cooler and fresher than the upstream profiles (red). Strong Ekman advection also extends to 58°S, potentially bringing much fresher and colder water into the formation area and contributing to the large winter Ekman fluxes observed here. As we have seen, eddy heat diffusion is weak (Fig. 14). However, the combination of strong lateral mixing upstream, and the slower circulation leaves more time for water masses to undergo the cooling, as shown for the our composite (Fig. 13).

Consider a schematic of the temporal evolution of a classical profile in the SAMW formation region during autumn/early winter (see Fig. 15), which is similar to our observed ARGO profiles. During autumn, the water column is weakly stratified, due to the upstream eddy mixing, with the remnants of the summer heating at the surface. In early winter (June), increased Ekman advection brings more cool, fresh surface water, which deepens and mixes due to the increased atmospheric cooling, but leaves a lens of saltier warm water just below the mixed layer. This spreading of cool fresh water across the SAF with a warmer and saltier subsurface is also observed at other sections farther east (Gordon and Molinelli 1982; Rintoul and Trull 2001).

As winter progresses, Ekman advection and the atmosphere cooling both increase to the point where a strong vertical circulation is induced just north of the front. The strong convection is sufficient to erode the weakened warm and salty lens, deepening the thermocline, leading to the deep winter mixed layers observed (see Fig. 15).

Summary and discussion

This study has used ARGO float data to estimate the heat balance in the surface mixed layer in the region of SAMW formation in the southeast Indian Ocean. We were able to observe the full seasonal cycle over a 2-year period, and our in situ data confirmed previous modeling and climatological studies that found out that air–sea fluxes plus Ekman fluxes dominate the surface heat budget (Ribbe 1999; Rintoul and England 2002; Speer et al. 1995). In the southeast Indian Ocean, we have quantified that the seasonal cycle of air–sea fluxes dominates the seasonal heat content variations in the mixed layer. Ekman fluxes continually cool the mixed layer, with an increased amplitude in winter of roughly −100 W m^{-2}.

One of the interesting results from this ARGO float analysis is how the subantarctic water masses evolve from west to east along the ACC axis, and the role of "upstream conditioning" on the formation of the deep winter mixed layers. Figure 5 clearly shows how the wide range of water mass properties upstream converges after the Kerguelen Plateau, leading to deeper mixed layers, which are cooler, fresher, and denser toward the east. Ekman forcing may be the dominant forcing downstream of Kerguelen, yet this term is as strong upstream of Kerguelen Plateau and the mixed layer remains at 100-m depth. It is the reversal of the eddy diffusion term upstream of Kerguelen that appears to be a key factor in de-stratifying the base of the mixed layer, and allowing the deeper winter mixed layers to develop downstream. This sudden strong cooling observed in the eddy heat diffusion parametrization is linked to the energetic eddy field, and the strong cross-frontal interleaving observed in the ARGO profiles occurs at the convergence of the fronts upstream of Kerguelen.

Although SAMW forms at many locations along the SAF (Hanawa and Talley 2001), the southeast Indian Ocean has

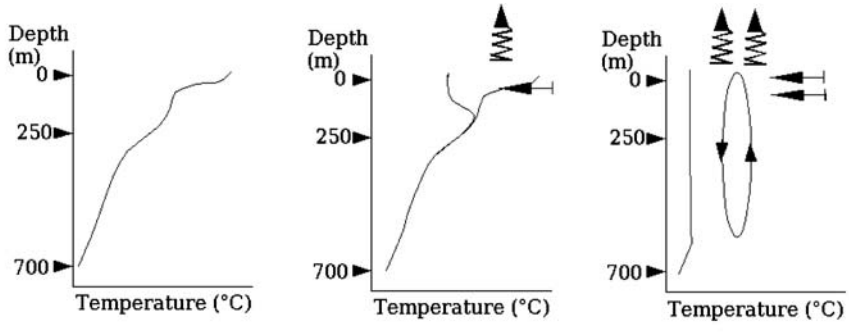

Month	May	June	July
Ekman intensity	-	+	++
Air Sea Fluxes	-	+	++

Fig. 15 Schematic of the temporal evolution of a temperature profile during autumn/early winter in the region of SAMW formation. In autumn (*left panel*) the temperature profile is well-stratified. As winter begins (*middle panel*), stronger Ekman advection of cold and fresh water reduces the temperature of the surface layer. A lens of warm and salty water remains just below the Ekman layer. As winter progresses (*right panel*), the Ekman advection and air sea cooling increase, destabilizing the surface layer and eroding the subsurface lens to create a deep mixed layer

the largest region with the deepest winter mixed layers and is a dominant source of SAMW. The particular combination of conditions upstream, illustrated in the schematic of Fig. 2, may make the formation process in the Indian Ocean more effective than elsewhere: a convergence of two strong dynamical fronts with an energetic eddy field around a large bathymetric barrier, the strong sudden cooling due to the eddy diffusion term, and the circumpolar maximum in mean wind forcing and Ekman heat transport. Downstream, the air–sea fluxes and Ekman transport are sufficient to explain the observed heat budget, but the deep mixed layers are evidently present because of the upstream conditions.

We have not explicitly included eddy diffusion or geostrophic advection in our downstream heat budget calculation, although we noted in Section 6.3 that these terms may be locally important for float pairs that are entrained in meanders of the SAF. We did estimate the diffusion and advection terms based on the available data sets. Eddy heat diffusion was calculated from surface drifter data and temperature fields; horizontal advection was calculated from altimetric data and temperature fields. However, when attempting to resolve fields dominated by strong mesoscale eddies, large errors were introduced whenever any of the components (e.g., currents and temperature) were slightly offset from one another in space and time. Close to the energetic SAF with strong currents and strong temperature gradients, we often have random values of order 1,000 W m^{-2}, but the net balance of terms is not calculated coherently. The large errors involved in the calculation led us to abandon the technique. The Ekman advection term, based on a larger scale forcing, is less affected by any spatiotemporal offsets in the two forcing components.

We have also seen from the stability analysis and the ARGO profiles that the haline component is important for the process of SAMW formation. The thermal destabilization at the base of the mixed layer is compensated by the fresh haline stratification (see Fig. 15). At present, we cannot calculate an accurate salt budget in the mixed layer due to the lack of high-resolution sea surface salinity data (equivalent to the satellite SST fields). However, the loss of salt and heat observed at the surface on the ARGO profiles is consistent with an Ekman advection from the South of cold and fresh water. Precipitation is thought to be of secondary importance compared to the Ekman contribution.

The sea surface salinity data are sparse, and spatial gradients are poorly resolved in the Southern Ocean by the climatological averages of SSS (Chaigneau and Morrow 2002), although this situation will be improved as more ARGO floats are deployed. Satellite salinity measurements will be available in the future from missions such as SMOS or Aquarius, but are not expected to be accurate at high latitudes (low temperatures) or available at mesoscale resolution.

Acknowledgements The ARGO data were collected and made freely available by the International ARGO Project and the national programs that contribute to it (http://www.argo.ucsd.edu, http://argo.jcommops.org). ARGO is a pilot program of the Global Ocean Observing System. This study was supported by the French PATOM and Coriolis programs and by NSF grants OCE 0336697 and OCE 0117618 to K. Speer.

Appendix

Appendix I: objective analysis of the float displacements

We obtained 8,849 velocity components from the ARGO database and 11,667 from the ALACE/PALACE database. We deduced from them the velocities at 400 m by adding the climatological shear between their drifting depth and 400 m. The velocities were averaged into 2° longitude by 1° latitude bins. Values formed by at least five data points are retained.

We mapped the velocity field and a stream function from the ARGO data in the southern Indian Ocean using an objective analysis following Gille (2003a).We seek an estimate $\widehat{\psi}$ of the true streamfunction ψ using the key relation:

$$\widehat{\psi} = P(A + \in I)^{-1}\phi \tag{3}$$

with:

$$P = \langle \phi, \psi \rangle \tag{4}$$

$$A = \langle \phi, \phi^T \rangle \tag{5}$$

where $\langle . \rangle$ is a scalar product, and Φ is a column vector containing all of the u and v measurements: $\Phi = [u_1, u_2, \ldots u_n, v_1, v_2, \ldots v_n]$. A is the covariance matrix of the measurement. We add an error $\in$ to its diagonal, which represents the effective increase in autocovariance due to measurement noise. This simplification assumes that the measurement noise is independent between two different positions and between u and v at the same position.

As shown by Gille and Kelly (1996), in the Southern Ocean we can apply a Gaussian correlation function in space. Gille (2003a) shows that an isotropic decorrelation scale of 495 km gives the best results for an objective analysis in the Southern Ocean. In this study, we chose an isotropic decorrelation scale of 400 km.

The mean 10-day current velocities estimated from ARGO data at the parking depth contain errors, mainly due

to the float drift at the surface. Furthermore, the float drift during the descent and ascent phase is also unknown. A study on the error in the drifting velocity at the float parking depth by Ichikawa et al. (2002) estimates this error to be between 10 to 25%. To be sure to overestimate this error, we chose 50% error level for the float velocities.

Appendix II: definition of the mixed layer depth

Accurate estimation of the mixed layer depth is a crucial part of the heat budget calculation. According to Thomson and Fine (2003), the threshold method with a finite difference criterion better approximates the "true" mixed layer depth, compared to the integral and regression methods. Experimental studies (see Brainerd and Gregg 1995) also find that the mixed layer depth based on a difference criterion is more stable because the gradient criterion method requires high-resolution profiles, which resolve the sharp vertical gradients. High-resolution in situ profiles are not always available, and ARGO profiles with a 10–20 m vertical resolution in the mixed layer cannot resolve sharp vertical gradients.

We chose to use a difference criterion method. The usual parameters used with this method are temperature and density; temperature is normally used when there is no equivalent salinity profiles. Most ARGO floats offer temperature and salinity profiles. We examined three different methods to find the mixed layer depth:

- a temperature difference criterion with a threshold 0.1°C; $\Delta T \leq 0.1$°C
- a density difference criterion with a threshold 0.01 kg m^{-3}; $\Delta\sigma \leq 0.01$ kg m^{-3}
- a density difference criterion with a threshold 0.03 kg m^{-3}; $\Delta\sigma \leq 0.03$ kg m^{-3}

The first measurement closest to the surface was chosen as the reference for each profile if this measurement is in the range from 0 to 10 m. If not the profile is rejected.

Consider first the difference between the two density criteria: $\Delta\sigma \leq 0.01$ and $\Delta\sigma \leq 0.03$. The results obtained by these two criteria are similar over most of the southern Indian Ocean (not shown). Nevertheless, some 3% of the profiles reveal mixed layer depths, which vary by more than 50%. When these exceptional profiles are examined, the 0.03 threshold is consistently associated with the mixed layer that we seek (i.e., the mixed layer depth for monthly averaged applications).

In the southern Indian Ocean, there are big differences in the mixed layer depth depending on whether we use the temperature or the density criteria. To visually highlight these differences, we calculated the average of the mixed depth layer in bins (2° latitude by 4° longitude) for each criterion and then mapped the differences. Figure 16 shows the difference between the method $\Delta T \leq 0.1$ and $\Delta\sigma \leq 0.03$.

South of the SAF, the $\Delta T \leq 0.1$ criterion shows a mixed layer depth far deeper than the density criteria; here there are small vertical temperature gradients but a strong halocline near the surface separating the fresh Antarctic Surface Waters from the saltier deep waters. In the region of mode water formation east of the Kerguelen Plateau between 80 and 120°E, the temperature criterion is shallower than the density criterion where the surface T–S compensates. Figure 16 also shows selected profiles in these two areas where there is a maximum depth difference between the two methods (ΔDepth>100 m). Clearly in both areas the density difference method is much better in identifying the mixed layer depth. For the following work, we will apply the 0.03-density criterion to find the mixed layer depth.

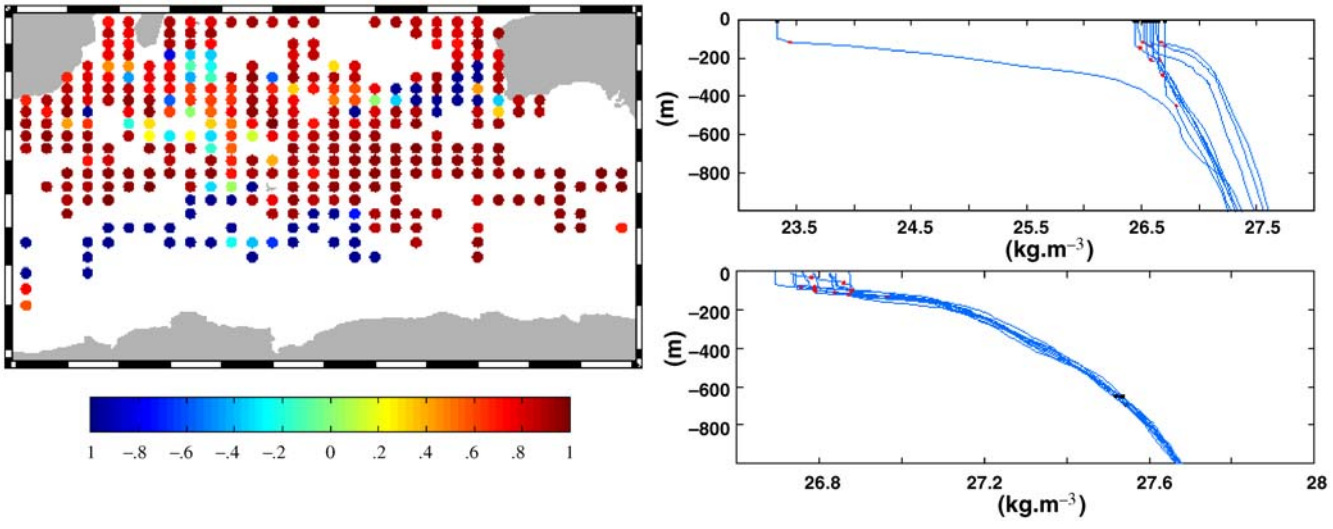

Fig. 16 *Left pannel* Normalized depth differences of the mixed layer depth identified by the $\Delta\sigma \leq 0.03$ and the $\Delta T \leq 0.1$ criteria. A negative difference occurs when the $\Delta T \leq 0.1$ criterion is shallower than the $\Delta\sigma \leq 0.03$ criteria. *Right panel* Selected density profiles in the region of mode water formation (*upper*) and south of the SAF (*lower*), which show large mixed layer depth differences using the density or temperature criteria. The *red points* correspond to the $\Delta\sigma \leq 0.03$ criterion and the *black points* correspond to the $\Delta T \leq 0.1$ criterion

Appendix III: detailed heat budget calculations

Ekman heat transport

For the advective term of the heat budget Eq. 1, **v** the horizontal mean velocity can be decomposed into the Ekman and geostrophic components as $\mathbf{v}=\mathbf{v_E}+\mathbf{v_g}$.The Ekman heat transport correspond to:

$$\int \mathbf{v}_E \cdot \rho C_p \nabla T dz$$

integrated over the mixed layer. Here

$$\mathbf{v}_E \cdot \nabla T$$

can be written:

$$\mathbf{v}_E \cdot \nabla T = u_E \frac{\partial T}{\partial x} + v_E \frac{\partial T}{\partial y} + w_E \frac{\partial T}{\partial z}$$

Assuming that the Ekman layer is included in the mixed layer, ρC_p has no dependency with the vertical and within the mixed layer $\frac{\partial T}{\partial z} = 0$. Thus:

$$\int_{EL} \mathbf{v}_E \cdot \rho C_p \nabla T dz = \rho C_p \left(U_E \frac{\partial T}{\partial x} + V_E \frac{\partial T}{\partial y} \right)$$

In the southern Indian Ocean, the Ekman transport is mainly northward (positive) with regard to the strong westerly winds, and ∇T is dominated by the strong (positive) meridional temperature gradient. So we expect $V_\mathrm{E} \frac{\partial T}{\partial y}$ to be much greater than $U_\mathrm{E} \frac{\partial T}{\partial x}$. Consequently, the Ekman induced heat flux can be approximated by $\rho C_\mathrm{p} V_\mathrm{E} \frac{\partial T}{\partial y}$. We note from this equation that a positive Ekman heat transport (as in our case) will induce a negative temperature tendency, or cooling. In other words, a positive Ekman heat transport can induce a negative effective Ekman heat flux at the base of the Ekman layer.

Heat content variations from ARGO floats

The heat content variation is calculated for each ARGO float within the formation region, using pairs of float profiles separated by 30 days (three float cycles) that remain in our zone. The temperature is integrated down to the deepest mixed layer depth, which occurs for the two profiles.

Because the floats do not identically sample the water column, every profile has been vertically interpolated onto a regular 10-db grid. The shallowest value of each profile has also been extended to the surface.

Several techniques were applied to evaluate the heat content variation. A first possibility was to calculate a mean temperature profile for every month, which was used to calculate a mean mixed layer depth and thus a mean heat content. This method shows a poor ability to represent the cycle of the wintertime enhanced convection and was not retained. Instead, we adopted a second method where all of the 30-day heat content variations available for the different floats were binned to form the monthly average.

For each 30-day heat content calculation, the forcing terms (Ekman and air sea fluxes) are interpolated onto the 10-day float positions and then averaged over the 30 days. In other words, considering four profiles from the same float, Ekman advection and air sea fluxes are interpolated onto the first, the second, and the third profile and then averaged, and the heat content variation is computed between the first and the fourth profile. The average of the forcing terms and the variation of the heat content are stored with the date of the fourth profile. The monthly averages shown in Figs. 8 and 10 are the average of all float pairs within the formation region whose fourth profile occurs during the given month.

One problem encountered with this calculation concerns the Lagrangian behavior of our floats. The heat budget calculation assumes a local change of the mixed layer in the same location, but for our calculation, the floats move between two samples. The movement of the float from one water mass to another introduces a change of heat content due to the float's advection. To assure that the floats remain in the same local area and water masses and to reduce this "relative advection," we developed a series of tests.

1. First, we elimated pairs of profiles when their difference in SST (considering time and position) was 1°C greater than the local change of SST (at the last profile position) during the same period. This reduces the effects of floats close to the SAF crossing large SST gradients due to meanders or eddies.
2. We also added a deep density criteria. If the difference between the density at 1,000 m is greater than 0.1 kg m^{-3}, we consider that the float doesn't sample the same water mass.
3. We also calculated the monthly rms of the forcing terms and of the ARGO heat content variation. We then removed the individual ARGO profiles whose value plus one rms lay outside the range of the forcing terms plus one rms. We visually checked that this criterion removed most profiles crossing the SAF.

The net effect of these tests was to eliminate 36% of data pairs.

References

Brainerd KE, Gregg MC (1995) Surface mixed and mixing layer depth. Deep Sea Res, Part II 42(A):1521–1543

Caldeira K, Duffy PB (2000) The role of the Southern Ocean in uptake and storage of anthropogenic carbon dioxide. Science 287:620–622

Chaigneau A, Morrow R (2002) Surface temperature and salinity variations between Tasmania and Antarctica, 1993–1999. J Geophys Res 107(C12):SRF22 1–9

Davis RE (1991) Observing the general circulation with floats. Deep Sea Res, Part II 38:S531–S571
Davis RE (2005) Intermediate-depth circulation of the Indian and South Pacific Oceans measured by autonomous floats. J Phys Oceanogr 35:583–707
Fine RA (1993) Circulation of Antarctic intermediate water in the South Indian Ocean. Deep Sea Res, Part I 40:2021–2042
Gill AE (1982) Atmosphere–ocean dynamics. Academic, New York
Gille ST (2003a) Float observations of the Southern Ocean: part 1. Estimating mean fields, bottom velocities, and topographic steering. J Phys Oceanogr 33:1167–1181
Gille ST (2003b) Float observations of the Southern Ocean: part 2. Eddy fluxes. J Phys Oceanogr 33:1182–1196
Gille ST, Kelly KA (1996) Scales of spatial and temporal variability in the Southern Ocean. J Geophys Res 101:8759–8773
Gordon AL, Molinelli EJ (1982) Southern ocean atlas. Columbia Univ. Press, New York, p 200
Hanawa K, Talley L (2001) In: Siedler G, Church J (eds) Ocean circulation and climate, chapter mode waters. International Geophysics Series, Academic, New York, pp 373–386
Ichikawa Y, Takatsuki Y, Mizuno K, Shikama N, Takeuchi K (2002) Estimation of drifting velocity and error at parking depth for the ARGO float. Technical report, Argo Technical Report, FY2001
Karstensen J, Quadfasel D (2002) Formation of Southern hemisphere thermocline waters: water mass conversion and subduction. J Phys Oceanogr 32:3020–3038
Keffer T (1985) The ventilation of the world's oceans: maps of the potential vorticity field. J Phys Oceanogr 15:509–523
Le Traon PY, Morrow R (2001) Satellite altimetry and earth sciences, chapter Ocean currents and eddies. Academic, New York, pp 171–215
MacCready P, Quay P (2001) Biological export flux in the Southern Ocean estimated from a climatological nitrate budget. Deep Sea Res, Part II 49:4299–4322
McCarthy MC, Talley LD (1999) Three-dimensional potential vorticity structure in the Indian Ocean. J Geophys Res 104:13251–13267
McCartney MS (1977) Subantarctic mode water. In: Angel M (ed) A voyage of discovery, Pergamon, New York, pp 103–119
McCartney MS (1982) The subtropical recirculation of mode waters. J Mar Res 40(suppl):427–464
Metzl N, Tilbrook B, Poisson A (1999) The annual fCO2 cycle and the air–sea CO2 flux in the sub-Antarctic Ocean. Tellus 51B:849–861
Nagata Y, Michida Y, Umimura Y (1988) Variation of position and structures of the oceanic fronts in the Indian Ocean sector of the Southern Ocean in the period from 1965 to 1987. In: D. Sahrhage (ed) Antarctic ocean and resources variability, Springer, Berlin Heidelberg New York, pp 92–98
Oh IS, Zhurbas V, Park W (2000) Estimating horizontal diffusivity in the East Sea (Sea of Japan) and the Northwest Pacific from satellite-tracked drifter data. J Geophys Res 105:6483–6492
Orsi AH, Whitworth T III, Nowlin WD Jr (1995) On the meridional extent and fronts of the Antarctic Circumpolar Current. Deep Sea Res, Part II 42:641–673
Qui B (2000) Interannual variability of the Kuroshio Extension system and its impact on the wintertime SST field. J Phys Oceanogr 30:1486–1502
Ribbe J (1999) On wind-driven mid-latitude convection in ocean general circulation models. Tellus 51A:505–516
Rintoul SR, England MH (2002) Ekman transport dominates air–sea fluxes in driving variability of Subantarctic Mode Water. J Phys Oceanogr 32:1308–1321
Rintoul SR, Trull TW (2001) Seasonal evolution of the mixed layer in the Subantarctic Zone south of Australia. J Geophys Res 106:31447–31462
Sabine C, Feely RA, Gruber N, Key RM, Lee K, Bulister JL, Wannikhof R, Wong CS, Wallace DWR, Tilbrook B, MIllero FJ, Peng T-H, Kozry A, Ono T, Rios AF (2004) The oceanic sink for anthropogenic co2. Science 305:367–371
Sandwell DT, Zhang B (1989) Global mesoscale variability from the Geosat Exact Repeat Mission: correlation with ocean depth. J Geophys Res 94:17971–17984
Sarmiento JL, Gruber N, Brezinski MA, Dunne JP (2004) High-latitude controls of thermocline nutrients and lowlatitude biological productivity. Nature 427:56–60
Sarmiento JL, Orr JC (1991) Three-dimensional ocean model simulations of the impact of Southern Ocean nutrient depletion on atmospheric CO2 and ocean chemistry. Limnol Oceangr 36:1928–1950
Schodlock MP, Tomczak M, White N (1997) Deep sections through the South Australian Basin and across the Australian–Antarctic discordance. Geophys Res Lett 24:2785–2788
Speer KG, Isemer HJ, Biastoch A (1995) Water mass formation from revised COADS data. J Phys Oceanogr 25:2444–2457
Stevenson JW, Niiler PP (1983) Upper ocean heat budget during the Hawaii to Tahiti Shuttle Experiment. J Phys Oceanogr 13:1894–1907
Stramma L (1992) The south Indian Ocean current. J Phys Oceanogr 22:421–430
Talley LD (1999) Antarctic intermediate water in the South formation of Subantarctic Mode Water in the southeastern Indian Ocean. In: Wefer G, Berger WH, Siedler G, Webb D (eds) The South Atlantic: present and past circulation, Springer, Berlin Heidelberg New York, pp 219–238
Thomson RE, Fine IV (2003) Estimating mixed layer depth from oceanic profile data. J Atmos Ocean Technol 20(2):319–329
Wong APS, Bindoff NL, Church J (1999) Large-scale freshening of intermediate waters in the Pacific and Indian oceans. Nature 400:440–443
Wong APS, Johnson G, Owens W (2003) Delayed-mode calibration of autonomous CTD profiling float salinity data by theta–S climatology. J Atmos Ocean Technol 20(2):308–318